ELSEVIER

Int. J. Therm. Sci. 41 (2002) 17–28

International
Journal of
Thermal
Sciences

Evolution of the two-phase flow in a vertical tube—decomposition of gas fraction profiles according to bubble size classes using wire-mesh sensors

Horst-Michael Prasser *, Eckhard Krepper, Dirk Lucas

Forschungszentrum Rossendorf e.V., P.O. Box 510119, 01314 Dresden, Germany

Received 24 November 2000; accepted 12 February 2001

Abstract

The wire-mesh sensor developed by the Forschungszentrum Rossendorf produces sequences of instantaneous gas fraction distributions in a cross section with a time resolution of 1200 frames per second and a spatial resolution of about 2–3 mm. At moderate flow velocities (up to 1–2 $\mathrm{m \cdot s^{-1}}$), bubble size distributions can be obtained, since each individual bubble is mapped in several successive distributions. The method was used to study the evolution of the bubble size distribution in a vertical two-phase flow. For this purpose, the sensor was placed downstream of an air injector, the distance between air injection and sensor was varied. The bubble identification algorithm allows to select bubbles of a given range of the effective diameter and to calculate partial gas fraction profiles for this diameter range. In this way, the different behaviour of small and large bubbles in respect to the action of the lift force was observed in a mixture of small and large bubbles. © 2002 Éditions scientifiques et médicales Elsevier SAS. All rights reserved.

Keywords: Two-phase flow; Gas-liquid flow; Bubble size measurement; Gas fraction measurement; Flow pattern; Wire-mesh sensors

1. Introduction

Forces acting on bubbles in a gas-liquid flow strongly depend on the bubble diameter. This is well known for the drag force, which was investigated by many authors. In the field of the so-called non-drag forces, which act perpendicular to the flow direction, there are still open questions. Recently, it was found, that the lift force changes its sign at some critical bubble diameter [1], e.g., in a vertical upwards pipe flow, small bubbles are moved towards the wall, while bubbles with a diameter greater than the critical migrate towards the centre of the tube. Concerning the other non-drag forces, i.e., the lubrication force and the turbulent dispersion force, there are also still needs to complete the models.

The experimental input for the study of these forces comes mainly from the observation of single bubbles. In this paper, we would like to introduce a method that allows to effectively analyse the motion of bubbles depending on their size in a multi-disperse flow. For this purpose, measurements with our wire-mesh sensor [2] in a vertical upwards flow were carried out. In [3] we presented a method to measure bubble size distributions by evaluating wire-mesh sensor data. Now, we will show, that the bubble identification algorithm can be used to decompose radial gas fraction profiles according to bubble size classes. Measurements taken at different distances from a gas injection show the evolution of the gas fraction profiles for different bubble size classes separately. This makes it possible to study the net motion of the bubbles in the direction perpendicular to the flow, and to check theoretical models of the non-drag forces in a realistic multi-disperse flow.

2. Experimental test facility

The methods described below will be demonstrated by means of experimental data obtained in a vertical pipe flow. Measurements were performed at the MTLOOP test facility [4], a two-phase flow test loop of the Institute of Safety Research. The loop was operated with an air–water mixture at atmospheric pressure and a temperature of 30 °C. A vertical test section (Fig. 1) with an inner diameter of 51.2 mm was used. Air was injected in the lower

---

* Correspondence and reprints.
E-mail address: prasser@fz-rossendorf.de (H.-M. Prasser).

PII: S1290-0729(01)01300-X

Nomenclature

A	cross sectional area	m^2
a	weight coefficient	1
D	diameter (pipe, bubble)	m
f_m	meas. frequency	Hz
g	gravity constant	$\mathrm{m{\cdot}s}^{-2}$
J	superficial velocity	$\mathrm{m{\cdot}s}^{-1}$
L	length, height	m
r	radius (variable)	m
R	radius (pipe, sensor)	m
t	time	s
V	volume	m^3
w	velocity	$\mathrm{m{\cdot}s}^{-1}$
x, y, z	coordinates	m

Greek symbols

ε	gas fraction	1
ρ	density	$\mathrm{kg{\cdot}m}^{-3}$
σ	surface tension	$\mathrm{kg{\cdot}s}^{-2}$

Index

Air	air
Bl	bubble
G	gas
i, j, k	indices
m	index of radial position
max	maximum, final value
min	minimum
n	bubble number
sensor	sensor
Water	water
0	initial value, origin

Other signs

Δ	difference
*	virtual

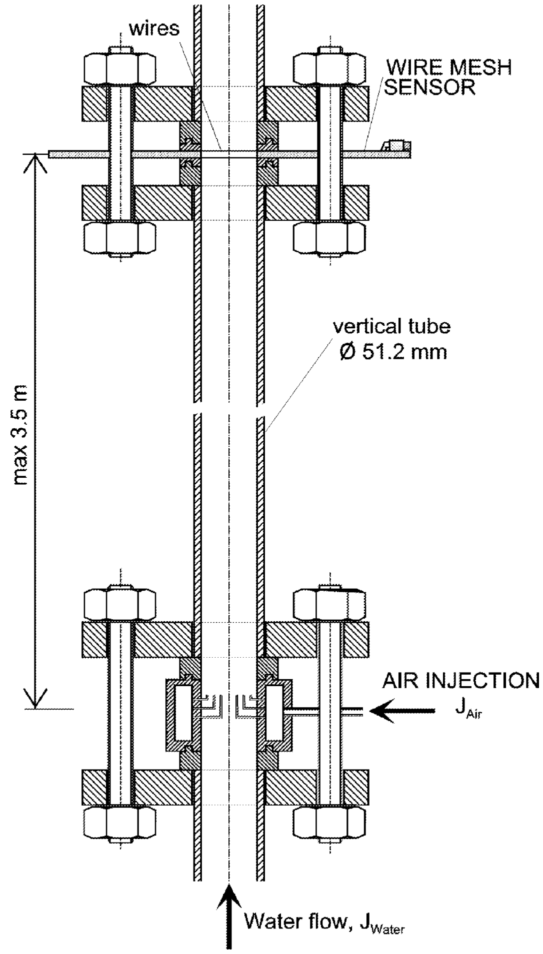

Fig. 1. Vertical test section equipped with air injection and wire-mesh sensor (schematic view, with air injection device A).

part of the test section. The kind of the gas injection was varied. The results presented in this paper were obtained by using of either 19 capillaries of 0.8 mm inner diameter, which were equally distributed over the cross section of the pipe (injection device A) or 8 orifices in the pipe wall of 4 mm inner diameter, equally distributed over the perimeter (injections device B). In the test loop, the superficial velocities can be varied between 0 and 12 $\mathrm{m{\cdot}s}^{-1}$ for air and 0 to 4 $\mathrm{m{\cdot}s}^{-1}$ for water, respectively. The air flow rate was measured under normal conditions. The superficial velocity was calculated from a flow rate corrected according to the actual temperature and pressure of the fluid. The tests were carried out under steady-state conditions.

The distance at which the wire mesh sensor was located above the injection device was varied from $L = 30$ mm to $L = 3133$ mm. Seven different relative inlet lengths (L/D) were specified: 0.6, 1.6, 2.5, 5, 10, 30, 60. Due to constructional constraints, the distance could only be approximated to the selected L/D ratios, i.e., the realised L/D ratios deviate from the specified. For some of the L/D ratios (5, 10, 30, 60) it was not possible to set up exactly the same distance for the two air injection devices. The measuring results are discussed according to the specified L/D ratios, which are, together with the real values, summarised in Table 1. In the course of the discussion it was assumed, that, for example, a measurement taken at $L = 3133$ mm with air injection A can be compared to a measurement taken at $L = 3033$ mm with air injection B.

Table 1
Geometrical conditions of the experiments

Parameter	air injection A	air injection B
type	capillary, equally distributed over pipe cross section	orifices in side wall of pipe, equally distributed over pipe perimeter
number	19	8
inner diameter	0.8 mm	4 mm

Distances between air injection and wire-mesh sensor

L/D	air injection A		air injection B	
specified	L (mm)	L/D (real)	L (mm)	L/D (real)
0.6	30	0.58	30	0.58
1.6	80	1.56	80	1.56
2.5	130	2.54	130	2.54
5	365	7.13	265	5.18
10	640	12.50	540	10.54
30	1632	31.88	1532	29.92
60	3133	61.19	3033	59.24

3. Primary measuring data of the wire-mesh sensor and data evaluation

3.1. Primary measuring data

The wire-mesh sensor consists of two electrode grids with 16 electrodes each (Fig. 2), put in flow direction behind each other. The local instantaneous electrical conductivity is directly measured between all pairs of crossing wires, a tomographic image reconstruction is not necessary. This results in 16 × 16 sensitive points, which are equally distributed over the cross section. In case of a tube diameter of 51.2 mm, this results in a spatial resolution of 3 mm, which equals the pitch of the electrode wires. From the 256 crossing points a number of 242 is available for measurements, some points in the corners are situated outside the circular cross section.

The sensor delivers a sequence of two-dimensional distributions of the local instantaneous conductivity, measured in each mesh formed by two crossing wires. Local instantaneous gas fractions are calculated assuming a linear dependence between gas fraction and conductivity. For this, the measured conductivity values are related to calibration values obtained for plain liquid in the measuring plane. The result is a three-dimensional data array $\varepsilon_{i,j,k}$ where k is the number of the instantaneous gas fraction distribution in the time sequence. The indices correspond to coordinates x, y of the local measurement in the cross section and the current time t in the following way:

$$\begin{aligned} x &= i \cdot \Delta x + x_0 \\ y &= j \cdot \Delta y + y_0 \\ t &= k \cdot \Delta t = \frac{k}{f_\mathrm{m}} \end{aligned} \qquad (1)$$

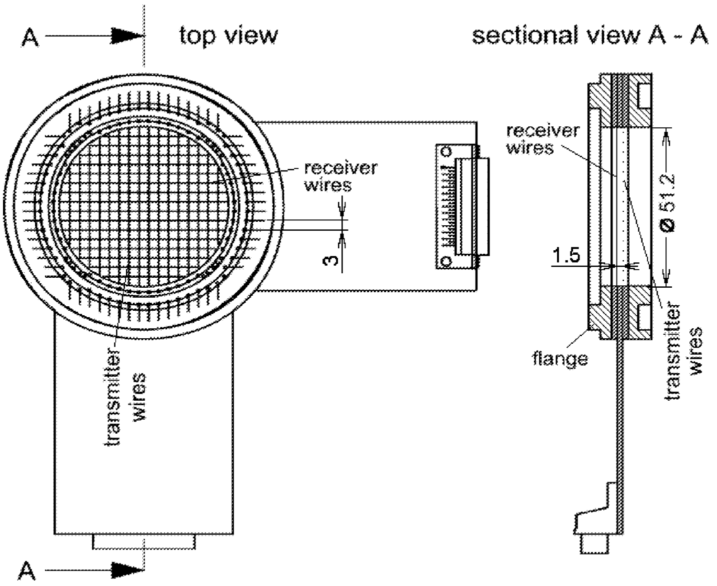

Fig. 2. Wire-mesh sensor with 2 × 16 electrodes.

Here, Δx and Δy denote the electrode pitches (in our case $\Delta x = \Delta y = 3$ mm), and f_m the measuring frequency ($f_\mathrm{m} = 1200$ Hz), and $\Delta t = 1/f_\mathrm{m}$ the time step, respectively, x_0 and y_0 are constants defining the origin of the coordinate system. Each individual value of $\varepsilon_{i,j,k}$ denotes to which extent the corresponding mesh $[i, j, k]$ is filled with the gaseous phase.

3.2. *Profiles of time-averaged gas fractions*

A time-averaged two-dimensional gas fraction distribution can be calculated as follows:

$$\overline{\varepsilon}_{i,j} = \frac{1}{k_\mathrm{max}} \cdot \sum_{k=1}^{k_\mathrm{max}} \varepsilon_{i,j,k} \tag{2}$$

where k_max is the number of instantaneous gas fraction distributions in the measuring sequence. A total average (void fraction) is obtained, when we average over the cross section:

$$\overline{\varepsilon} = \frac{1}{k_\mathrm{max}} \cdot \sum_{i=1}^{i_\mathrm{max}} \sum_{j=1}^{j_\mathrm{max}} \sum_{k=1}^{k_\mathrm{max}} a_{i,j} \cdot \varepsilon_{i,j,k} = \sum_{i=1}^{i_\mathrm{max}} \sum_{j=1}^{j_\mathrm{max}} a_{i,j} \cdot \overline{\varepsilon}_{i,j} \tag{3}$$

here i_max and j_max are the total numbers of electrode wires in both directions, $a_{i,j}$ are weight coefficients reflecting the contribution of the area of the given mesh $[i, j]$ to the total cross sectional area A_sensor. In the central region of the sensor holds $a_{i,j} = \Delta x \cdot \Delta y / A_\mathrm{sensor}$, while at the periphery the weight coefficients are less, because it has to be considered that a certain part of the given mesh is outside the circular cross section border of the sensor (Fig. 3). Elements which are completely located outside the border of the sensor obtain weight coefficients equal zero.

Radial profiles can be calculated by dividing the radius into m intervals and introducing a radial step width $\Delta r = R_\mathrm{sensor}/m$ and averaging $\overline{\varepsilon}_{i,j}$ over a ring-shaped domain, covering the radial interval $(m - 1/2) \cdot \Delta r \leqslant r \leqslant (m + 1/2) \cdot \Delta r$, Fig. 4. This is done using weight coefficients $a_{i,j,m}$, which characterise the common area of the mesh with the indices $[i, j]$ and the ring with the number m and the central radius $m \cdot \Delta r$, related to the total cross section of the sensor A_sensor. The averaging can then be written as follows:

$$\overline{\varepsilon}_m = \frac{1}{k_\mathrm{max}} \cdot \sum_{i=1}^{i_\mathrm{max}} \sum_{j=1}^{j_\mathrm{max}} \sum_{k=1}^{k_\mathrm{max}} a_{i,j,m} \cdot \varepsilon_{i,j,k} = \sum_{i=1}^{i_\mathrm{max}} \sum_{j=1}^{j_\mathrm{max}} a_{i,j,m} \cdot \overline{\varepsilon}_{i,j} \tag{4}$$

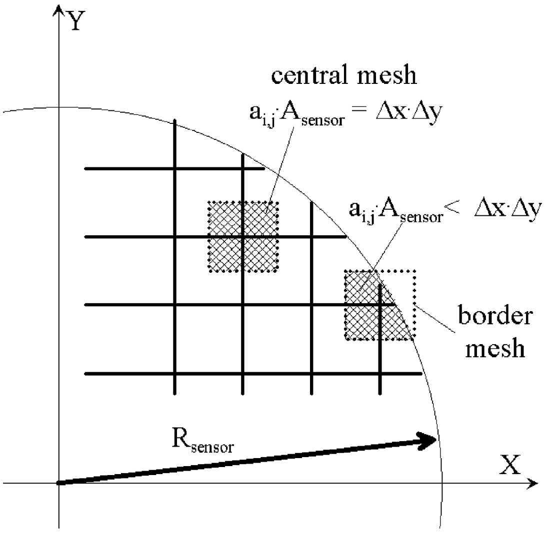

Fig. 3. Weight coefficients $a_{i,j}$ for averaging the gas fraction in the measuring cross section.

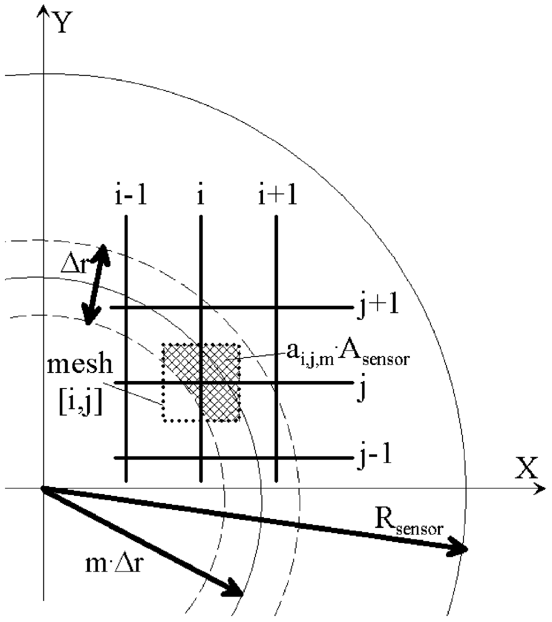

Fig. 4. Weight coefficients $a_{i,j,m}$ for calculating radial gas fraction profiles.

The determination of the weight coefficients is based on simple geometric calculations, which does not require more detailed description.

3.3. *Bubble size measurement*

The task to obtain bubble size distributions is solved in the following steps:

- Identification of bubbles, i.e., assigning each element $[i, j, k]$ either to one of N bubbles or to the area occupied by the plain liquid phase,
- integrating the local instantaneous gas fraction over the elements belonging to the given bubble to obtain the bubble volume and transfer to an equivalent diameter,
- calculation of a statistical distribution with the equivalent bubble diameter as variable.

For the first step, a bubble identification array $b_{i,j,k}$ of the same dimensions as $\varepsilon_{i,j,k}$ is defined. Before the start of the algorithm, a bubble counter is set to one and all elements of the bubble identification array $b_{i,j,k}$ are set to zero (“unlabelled”). Then a program loop is entered, in which the first action is the search of a local maximum among the unlabelled elements of the gas fraction distribution $\varepsilon_{i,j,k}$. This is the start element for a so-called recursive fill procedure. This procedure labels the corresponding element in the bubble identification array by assigning the current value of the bubble counter, if the local instantaneous gas fraction is still greater than the start value minus a differential threshold. The procedure furthermore includes recursive calls with the indices of all elements being the neighbours of the just treated element. When the run of this procedure is terminated, a continuous area in the array $b_{i,j,k}$ is filled with the current value of the bubble counter. Afterwards, the bubble counter is increased by 1 and the procedure is repeated by searching the next not labelled element with a gas fraction maximum. In this way cores of bubbles are identified. At the periphery of these cores there are still elements which were not labelled because the local gas fraction is lower than the threshold, since they were only partially covered by the bubble. These elements are subsequently assigned to the already existing bubbles without increasing the bubble counter. This approach guarantees a low number of unrealistic unifications of neighbouring bubbles as well as a low probability of unrealistic fragments which may be caused by the signal noise [3].

In the result, in the bubble identification array $b_{i,j,k}$ clusters of elements containing the same bubble number are formed. These clusters represent the three-dimensional regions occupied by the bubble with the corresponding number. The calculation of bubble volumes is carried out by integrating over the elements belonging to such a cluster:

$$V_{\mathrm{Bl},n} = \Delta x \cdot \Delta y \cdot \Delta t \cdot \sum_{\forall i,j,k:\ n=b_{i,j,k}} w_{\mathrm{G},i,j,k} \cdot \varepsilon_{i,j,k} \tag{5}$$

If, as a matter of rule, the instantaneous local gas velocities $w_{\mathrm{G},i,j,k}$ are not available, we use the average gas phase velocity $\overline{w_{\mathrm{G}}} = J_{\mathrm{G}}/\overline{\varepsilon}$, which is a satisfying approximation in a turbulent upwards pipe flow. In this case equation (5) can be written as:

$$V_{\mathrm{Bl},n} \cong \overline{w_{\mathrm{G}}} \cdot \Delta x \cdot \Delta y \cdot \Delta t \cdot \sum_{\forall i,j,k:\ n=b_{i,j,k}} \varepsilon_{i,j,k} \tag{6}$$

From the bubble volumes, equivalent bubble diameters are calculated:

$$D_{\mathrm{Bl},n} = \sqrt[3]{\frac{6}{\pi} \cdot V_{\mathrm{Bl},n}} \tag{7}$$

A detailed description of the bubble size measurement method including an analysis of the accuracy of the bubble imaging, the bubble size measurement and an assessment of the flow disturbance caused by the sensor is given in [3].

It has to be remarked that more than one small bubbles appearing in one mesh of the sensor in the same time cannot be resolved, i.e., they are identified as one bubble, while a single bubble can be detected even if the size is smaller than the electrode pitch. The lower limit results from the noise level of the conductivity measurement. It is about 2 mm in case of the presented results, which is sufficient since the characteristic bubble sizes in the investigated air-water system are much higher.

3.4. *Decomposition of gas fraction distributions according to bubble size classes*

After the bubble identification procedure and the calculation of bubble diameters according to equations (6) and (7) is completed, bubble numbers are assigned to each element in the gas fraction distribution $\varepsilon_{i,j,k}$, stored in the corresponding element of the bubble identification array $b_{i,j,k}$. Furthermore, each bubble number refers to an equivalent bubble diameter. It can therefore easily checked if an element $\varepsilon_{i,j,k}$ of the gas fraction distribution belongs to a bubble, the diameter of which lies within a given interval of $D_{\min} \leqslant D_{\mathrm{Bl}} < D_{\max}$. A new array of decomposed gas fractions $\varepsilon'_{i,j,k}$ can be created as follows:

$$\varepsilon'_{i,j,k} = \begin{cases} \varepsilon_{i,j,k} & \text{if } b_{i,j,k} \neq 0 \text{ and} \\ & D_{\min} \leqslant D_{\mathrm{Bl},b_{i,j,k}} < D_{\max} \\ 0 & \text{(otherwise)} \end{cases} \tag{8}$$

This operation can be repeated for an arbitrary set of bubble size classes. In this way, the initial distribution is decomposed according to the given bubble size classes.

The procedure is illustrated in Fig. 5 on the basis of virtual sectional views of the instantaneous gas fraction distributions. To create these virtual sectional views, a time sequence of instantaneous distributions over the tube diameter is plotted in a vertical column. The time axis was transformed into a virtual z^*-axis by means of the average gas phase velocity, i.e., $z^* = \overline{w_{\mathrm{G}}} \cdot \Delta t$. Height and width of the resulting columns correspond to the same geometric scale, so that the bubbles are displayed in their realistic shape (with the accuracy of the velocity assumption).

The upper left column in Fig. 5 represents a virtual sectional side view of the sequence of gas fraction distributions measured by the sensor. On the right side the bubble size distribution is plotted. The column below the virtual sectional view of the primary data is the result of colouring the bubbles according to their diameter: if the diameter is less than 5.5 mm, they were painted green, in the opposite case red. Now, the initial sequence can be divided in sequences of gas fraction distributions considering only bubbles with $D_{\mathrm{Bl}} < 5.5$ mm (column with only green bubbles) and $D_{\mathrm{Bl}} > 5.5$ mm (column with only red bubbles).

Radial profiles of the part of gas fraction carried by bubbles that belong to a given interval of effective diameters can be obtained by averaging the corresponding partial local instantaneous gas fractions $\varepsilon'_{i,j,k}$ applying Eq. (4).

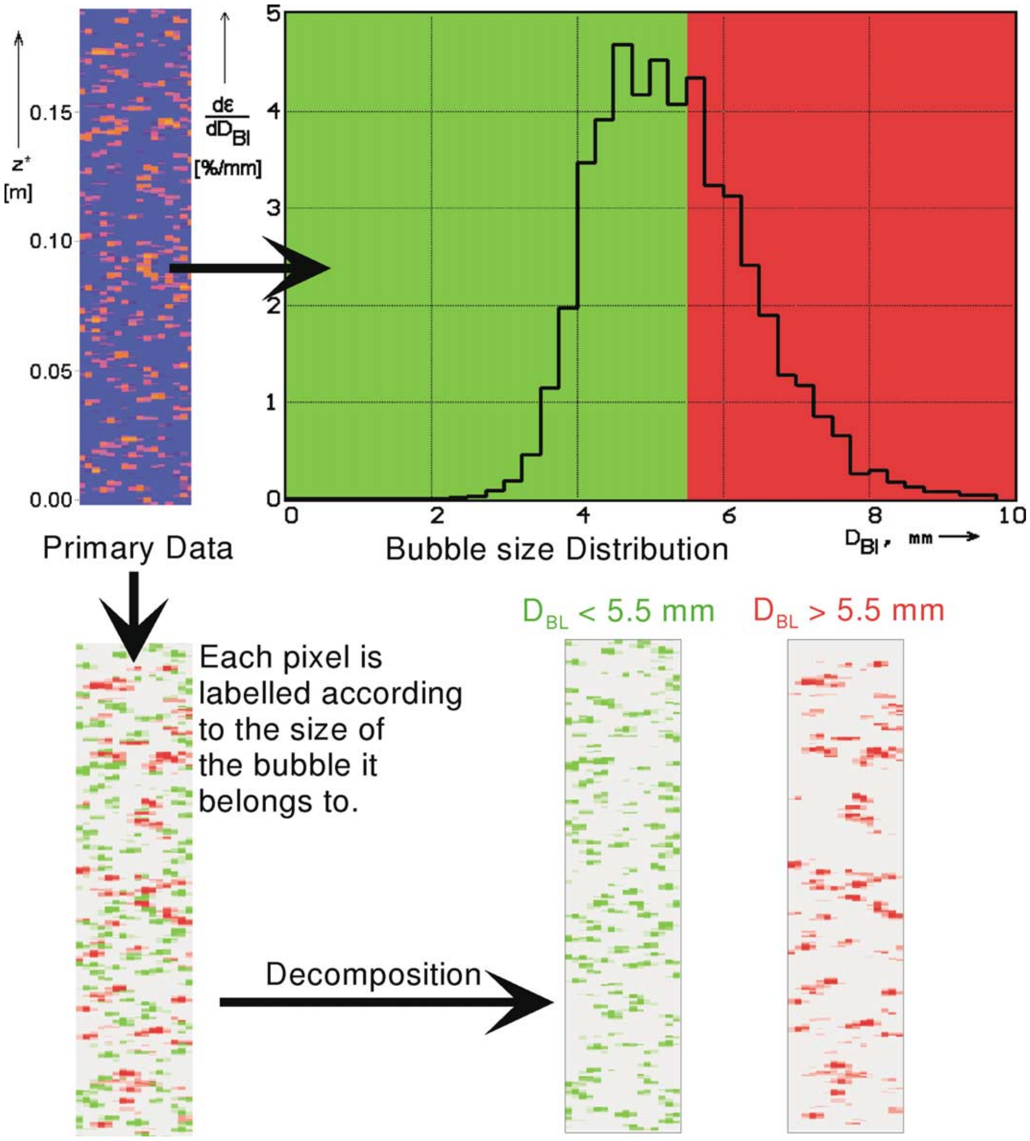

Fig. 5. Decomposition of gas fraction distributions according to the bubble size, $J_{\mathrm{Water}} = 0.4\ \mathrm{m \cdot s^{-1}}$, $J_{\mathrm{Air}} = 0.06\ \mathrm{m \cdot s^{-1}}$, $L/D \cong 60$.

4. Experimental results on the evolution of the structure of the two-phase flow

4.1. *Influence of the primary bubble size on the evolution of gas fraction profile*

For the analyses of the flow regimes discussed below data sets of a measuring period of 10 s recorded at a measuring frequency of $f_{\mathrm{m}} = 1200$ Hz were used. This means both radial gas fraction profiles and bubble size distributions were calculated from sets of $k_{\max} = 12000$ successive instantaneous gas fraction distributions in the measuring cross section.

In Fig. 6 measuring results for a low air flow rate are shown, where bubble coalescence does not play an important role. In this case, the use of the gas injection device A exclusively led to primary bubble diameters of less than 5.5 mm, while all generated bubbles were larger than 5.5 mm when the gas was injected through the orifices of 4 mm diameter (device B) (Fig. 6(a)). The bubble diameter of 5.5 mm is just the critical value found by Tomiyama [1], where the lift force changes its sign when the liquid is water at room temperature. The evolution of the gas fraction profiles calculated according to Eq. (4) are shown in Fig. 6(b).

In case of the equally distributed capillaries small primary bubbles are generated in the entire cross section. Nevertheless, already at the relative distance of $L/D \cong 0.6$ a pronounced wall-peak of the gas fraction profile is found. This is caused by the lift force acting in the direction towards the wall in an upwards bubble flow. When the wall orifices are used, a wall peak is formed due to the peripheral air injection. In this case the primary bubbles are all larger than 5.5 mm and the reversed lift force causes the bubbles to move towards the axis of the pipe. At $L/D \cong 60$ a central peak

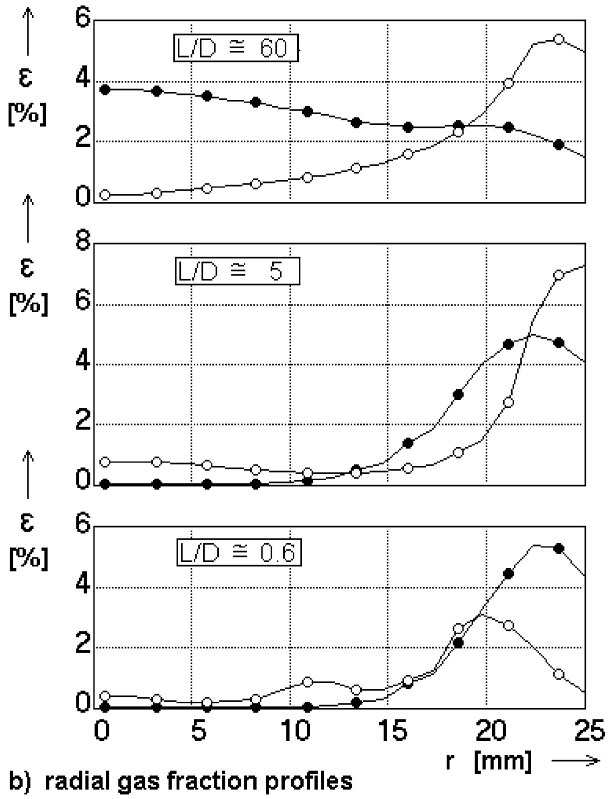

b) radial gas fraction profiles

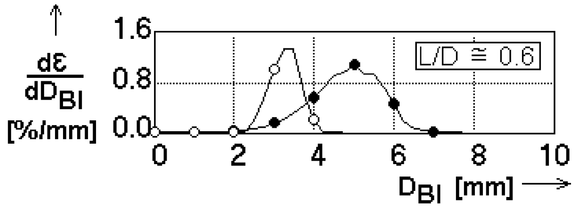

a) primary bubble size distribution

Fig. 6. Primary bubble size distributions and the evolution of radial gas fraction profiles at superficial velocities of $J_{\mathrm{Water}} = 1\ \mathrm{m{\cdot}s^{-1}}$ and $J_{\mathrm{Air}} = 0.02\ \mathrm{m{\cdot}s^{-1}}$ (absence of significant coalescence).

has established. These measurements confirm the findings of Tomiyama [1], which were obtained by observing the rise of single bubbles of well defined volume.

4.2. *Influence of the primary bubble size on the evolution of bubble size distributions*

Another interesting observation was done when the superficial air velocity was increased to $J_{\mathrm{Air}} = 0.125\ \mathrm{m{\cdot}s^{-1}}$. In this case the mode of air injection decided whether the bubble size distribution remained narrow with a maximum near the primary bubble diameter or whether an intensive bubble coalescence and fragmentation occurred (Fig. 7). In case of injection device A the primary bubbles were in the range of $D_0 = 4$ mm. Along the pipe, the maximum of the bubble size distribution remained unchanged. Nevertheless, some coalescence occurred leading to the appearance of a second peak at a diameter of $D = \sqrt[3]{2} \cdot D_0$, which is the result of coalescence events between pairs of bubbles of the initial size.

The air injection device B generated much larger bubbles. The primary diameter is about 8 mm. Though the superficial velocities were kept identical in both cases, the flow in the second case is dominated by coalescence leading to the appearance of large bubbles with equivalent diameters of up to 30 mm. Obviously, the flow regime was close to the bubble-slug transition. On the other hand, there was a generation of bubbles smaller than the primary bubbles. At $H \cong 3000$ mm ($L/D \cong 60$) the maximum of the bubble size distribution was at approximately $D_{\mathrm{Bl}} = 5$ mm.

This experiment has shown that coalescence and fragmentation depends on the size of the primary bubbles. Large bubbles generate more intensive turbulent wakes. Furthermore, starting with an Eötvös Number of about 1 they start to perform oscillatory motions. These might be the reasons for the more intensive coalescence. On the other hand, they can be easier fragmented, mainly because they are more deformed in turbulent flow fields and sheer regions than small ones, which is again connected with the Eötvös number (The Eötvös number $Eo = g(\rho_{\mathrm{Water}} - \rho_{\mathrm{Air}})D_{\mathrm{BL}}^2/\sigma$ puts into relation buoyancy and surface forces acting at the bubble. With increasing Eötvös number the surface tension looses influence and the bubble shape starts to deviate from spherical).

It is worth to remark that the flow pattern is still completely different at the end of the test section. An inlet length of $L/D \cong 60$ is obviously not sufficient to establish equilibrium conditions at the mentioned superficial velocities.

If the air flow rate is increased to $J_{\mathrm{Air}} = 0.5\ \mathrm{m{\cdot}s^{-1}}$ (at the same superficial water velocity as in Figs. 6 and 7), the more intensive turbulisation by the gas phase causes a faster establishing of the equilibrium. In the result, the bubble size distributions generated by the injecting devices A and B rapidly converge and the bubble size distribution at $L/D\ H \cong 60$ is almost independent of the primary bubble size (Fig. 8).

4.3. *Results of the decomposition of gas fraction profiles according to bubble size classes*

The decomposition of radial gas fraction profiles described in Section 3.4 was applied to data obtained in an experiment with an air injection through the equally distributed capillaries (injection device A) at superficial velocities of $J_{\mathrm{Water}} = 0.4\ \mathrm{m{\cdot}s^{-1}}$ and $J_{\mathrm{Air}} = 0.06\ \mathrm{m{\cdot}s^{-1}}$. The inlet length was again varied from $L/D \cong 0.6$ to $L/D \cong 60$. The measured bubble size distribution at $L/D \cong 0.6$ indicates, that all primary bubbles have an equivalent diameter smaller than 5.5 mm (Fig. 9, right side).

With increasing distance between air injection and sensor, the progressing bubble coalescence leads to the generation

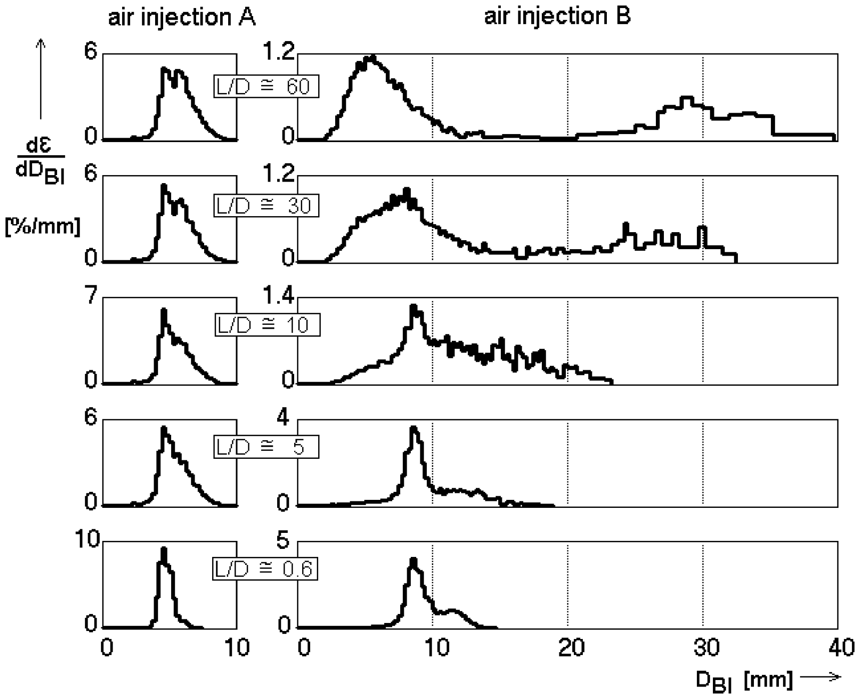

Fig. 7. Evolution of the bubble size distribution along a vertical tube, $J_{\text{Air}} = 0.125$ m·s, $J_{\text{Water}} = 1$ m·s^{-1}, A — 19 capillaries, $D = 0.8$ mm, B — 8 wall orifices, $D = 4$ mm.

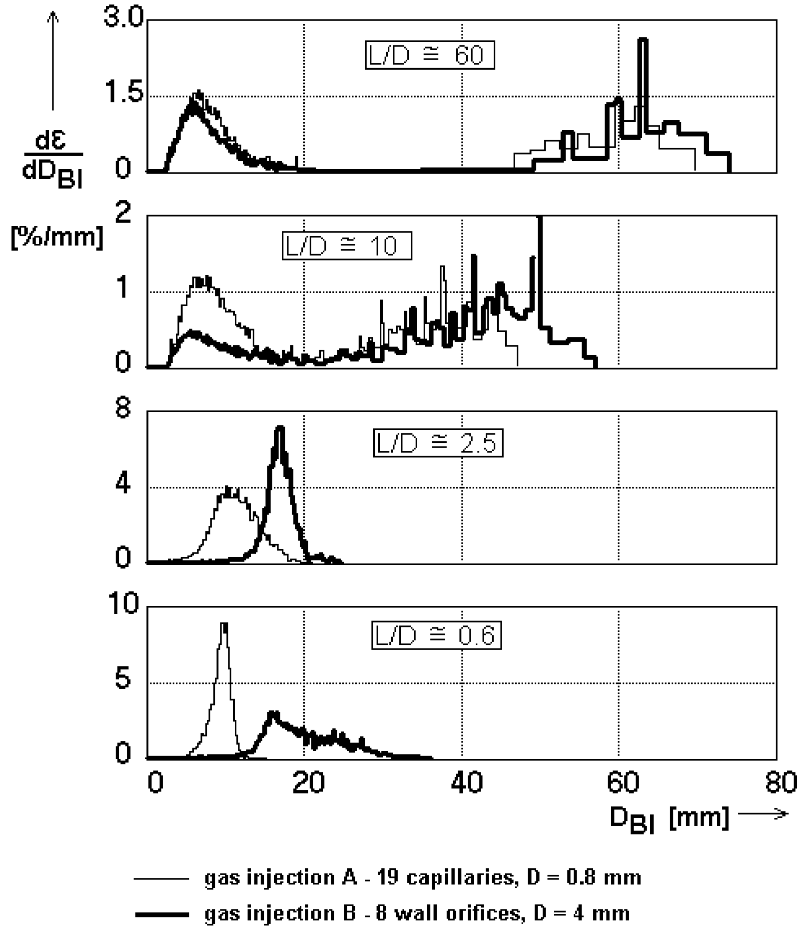

Fig. 8. Evolution of the bubble size distribution along a vertical tube, $J_{\text{Air}} = 0.5$ m·s^{-1}, $J_{\text{Water}} = 1$ m·s^{-1}, A — 19 capillaries, $D = 0.8$ mm, C — 8 wall orifices, $D = 4$ mm.

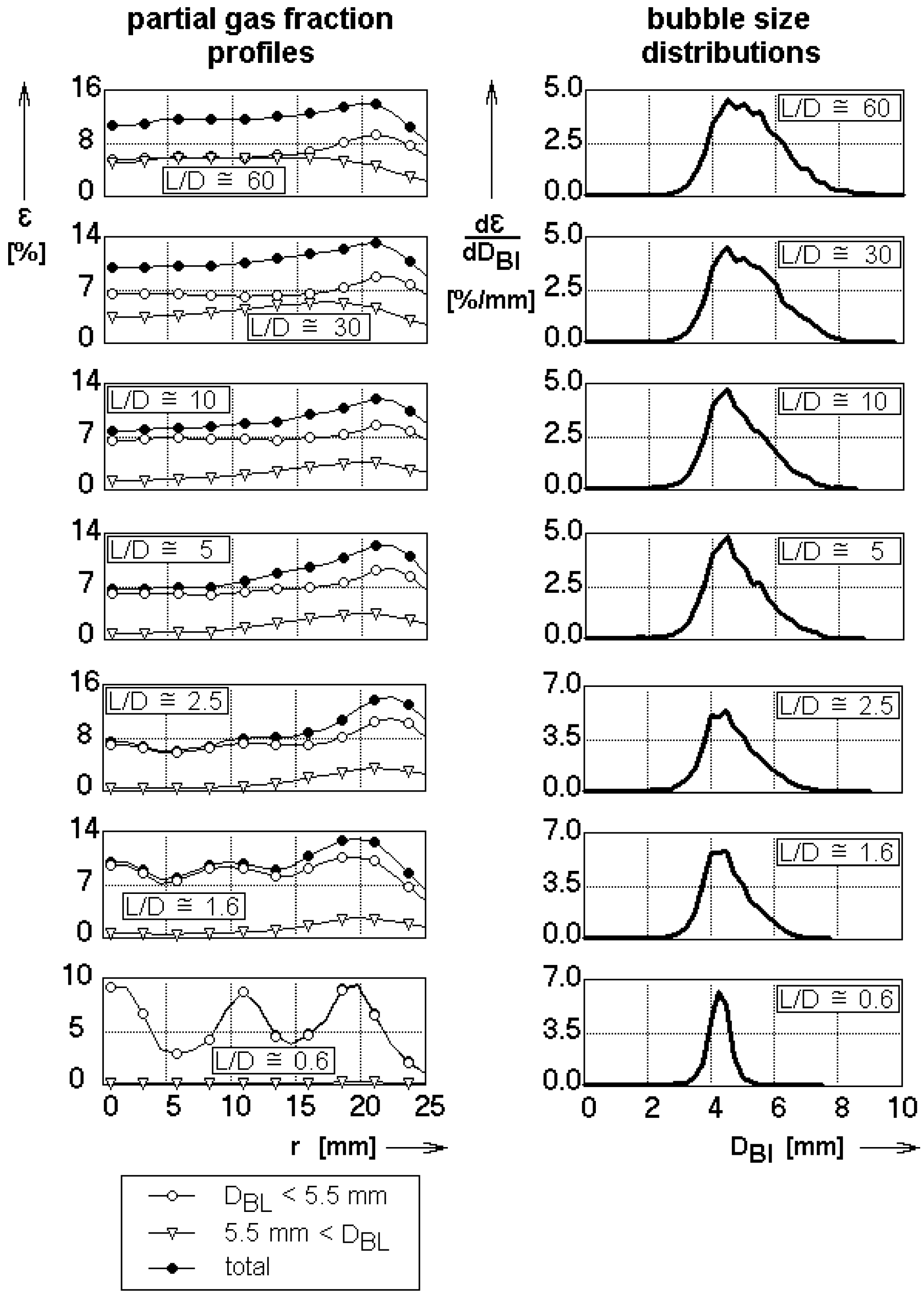

Fig. 9. Evolution of partial gas fraction profiles and bubble size distributions along the pipe, $J_{\text{Water}} = 0.4\ \text{m}\cdot\text{s}^{-1}$, $J_{\text{Air}} = 0.06\ \text{m}\cdot\text{s}^{-1}$, air injection device A — 19 eqally distributed capillaries, ∅0.8 mm.

of bubbles greater than 5.5 mm. When we look at the decomposed radial gas fraction profiles (Fig. 9, left side), the tendency of the small bubble fraction to move towards the wall is clearly visible. At $L/D \cong 0.6$, the profile is still strongly determined by the gas fraction maxima found at the places where the capillaries are located. With growing distance, the gas fraction represented by the small bubble fraction shifts towards the wall. The increase of gas fraction near the wall leads to an intensification of coalescence and a generation of bubbles with $D_{\text{Bl}} > 5.5$ mm in this region. These bubbles experience an inverse lift force, pushing them towards the center of the pipe. At $L/D \cong 60$ the equilibrium is nearly established. Here, we observe a pronounced wall peaking of the total gas fraction profile, caused by the peak of the partial gas fraction of the small bubble class. The large bubbles ($D > 5.5$ mm) tend to form a central maximum.

A similar experiment at identical superficial velocities was carried out with the injection of air through the injecting device B (8 wall orifices of 4 mm diameter). In this case, the primary bubbles are larger than 5.5 mm. Close above the

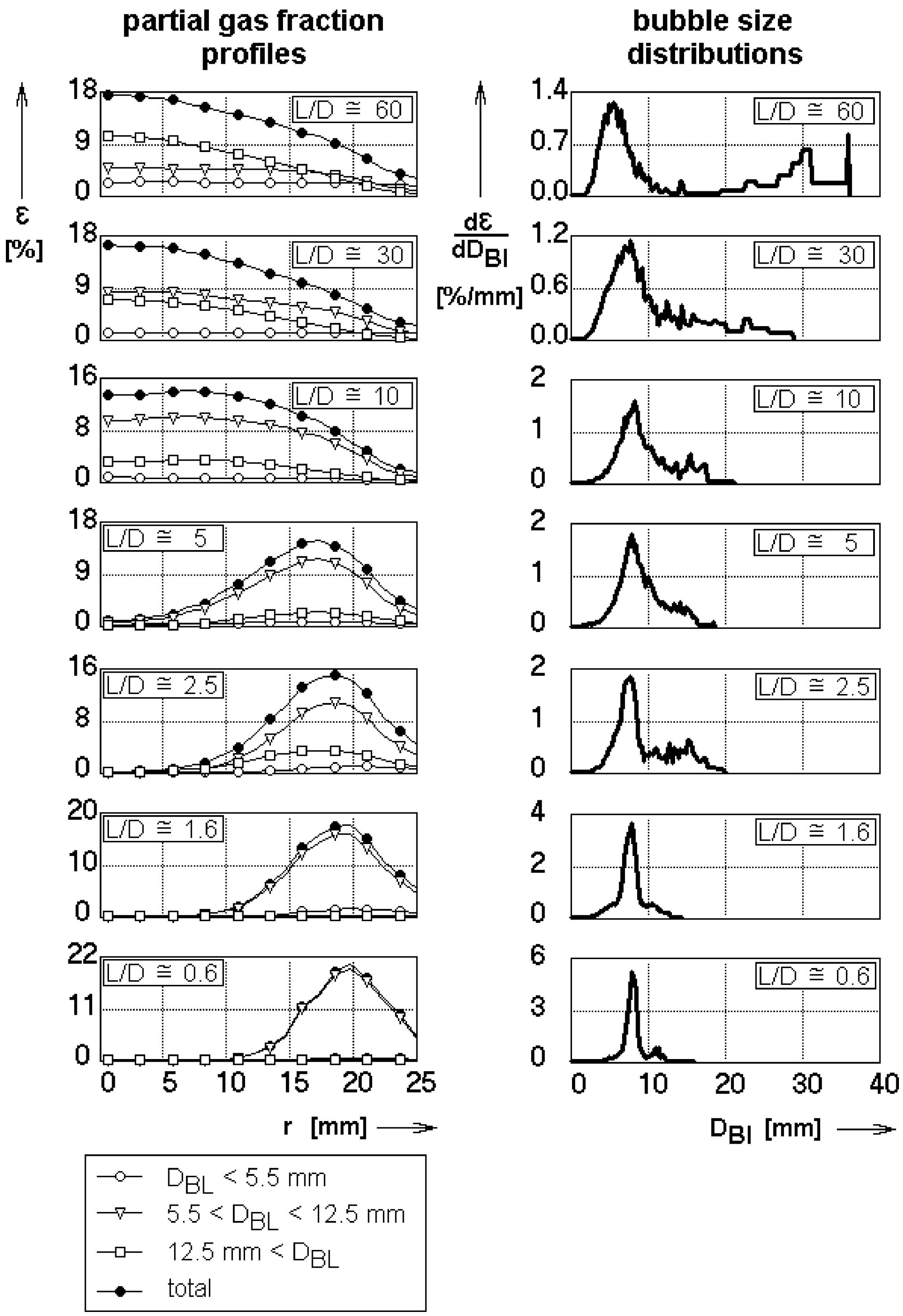

Fig. 10. Evolution of partial gas fraction profiles and bubble size distributions along the pipe, $J_{\mathrm{Water}} = 0.4\ \mathrm{m{\cdot}s^{-1}}$, $J_{\mathrm{Air}} = 0.06\ \mathrm{m{\cdot}s^{-1}}$, air injection device B — 8 orifices in the side wall, ∅4 mm.

injection they are found at the periphery of the pipe (Fig. 10), since they have been generated at the wall. With growing distance, a generation of both bubbles smaller than 5.5 mm and larger that 12.5 mm is observed.

Since bubbles with a diameter less than 5.5 mm are not generated at the gas injection orifices, they must be the result of fragmentation events. In the same time bubble coalescence leads to the appearance of bubbles larger than 12.5 mm. The bubbles of both classes of large bubbles (5.5 mm $\leqslant D_{\mathrm{Bl}} \leqslant$ 12.5 mm and 12.5 mm $\leqslant D_{\mathrm{Bl}}$) are quickly shifted to the center of the pipe. At the end of the test section, the class of small bubbles does not show the expected wall

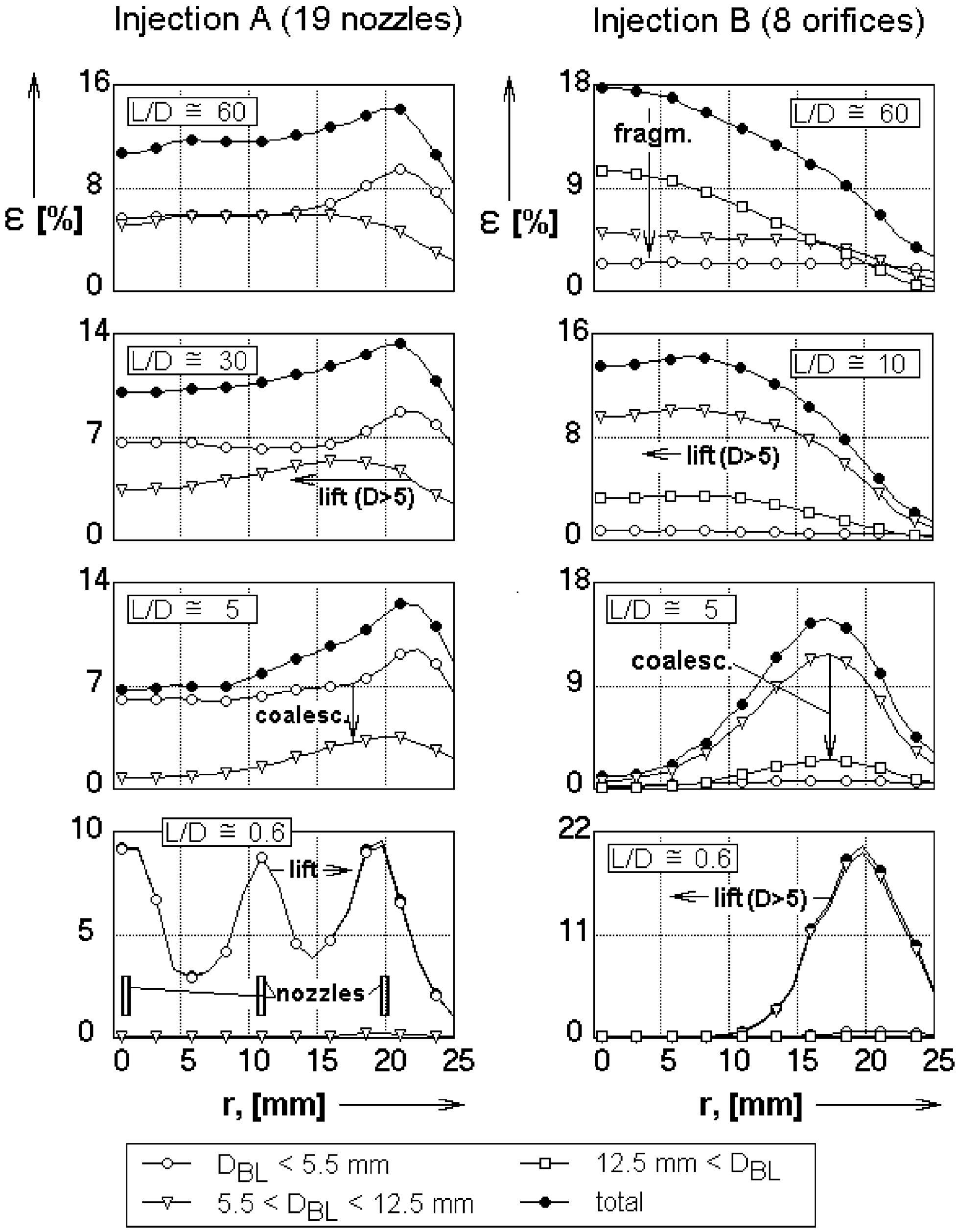

Fig. 11. Effect of coalescence and lift force to the evolution of gas fraction profiles.

peaking just because the fragmentation process is generating a large number of small bubbles in the center of the pipe, where the gas fractions are high. The more equal distribution of the small bubbles in comparison to the large bubble fractions is a hint to the tendency of the small bubble to move towards the wall.

A bimodal bubble size distribution characteristic for the transition from bubble to slug flow is established at the end of the test section. The inverse lift force transports the large bubbles to the centre of the pipe. The effect of coalescence, fragmentation and lift force is marked in Fig. 11 for both injection devices.

Again, the flow structure in the two examples compared in Fig. 11 is not identical at the end of the test section, though identical superficial velocities of gas and liquid were present (see Fig. 7). Obviously, an inlet length of $L/D \cong 60$ is still not sufficient to establish an equilibrium between bubble fragmentation and coalescence as well as with regard to the lateral movement of the bubbles. The flow pattern is still influenced by the kind of gas injection.

5. Conclusion

The wire-mesh sensor is able to provide detailed information about the structure of the two-phase flow. It is successfully used to visualise the air-water flow in a vertical pipeline. From the primary measuring data it is possible to obtain void fraction profiles as well as bubble size distributions. Experiments were carried out to study the evolution of the flow structure with growing distance from the gas injection. The bubble size distributions clearly show the effect of coalescence and fragmentation.

At certain combinations of the superficial velocities of gas and liquid (e.g., at $J_{\mathrm{Air}} = 0.125\ \mathrm{m{\cdot}s^{-1}}$, $J_{\mathrm{Water}} = 1\ \mathrm{m{\cdot}s^{-1}}$), the size of the primary bubbles is of crucially importance for the evolution of the flow pattern. The tendency of increasing coalescence frequency with growing bubble diameter may be so dominating, that even an inlet length of $L/D \cong 60$ was not sufficient to establish an equilibrium bubble size distribution, i.e., the bubble size distributions were still strongly depending from the primary bubble size despite of identical gas fractions. At higher superficial gas velocities (e.g., at $J_{\mathrm{Air}} = 0.5\ \mathrm{m{\cdot}s^{-1}}$) the bubble size distribution becomes independent from the gas injection device.

The decomposition of radial gas fraction profiles according to bubble-size classes allows to study lift force effects. The difference in the behaviour of small and large bubbles in connection with the change in sign of the lift force, which was predicted by Tomiyama [1], was observed by the new measuring method in a realistic multi-disperse two-phase flow.

The results have furthermore shown, that the coalescence intensity depends from the local gas fraction. In case of the injection of bubbles small enough to be driven towards the wall, the formation of large bubbles starts in the layer close to the pipe wall, where the gas fraction distribution develops the well-known wall peak. The generated large bubbles experience an inverse lift force and are travelling towards the centre. In case of a high enough gas fraction in the center, there can be a source of small bubbles in the central region, which afterwards start to move in direction towards the wall. Theoretical models must therefore consider the different radial profiles of the gas fraction represented by different bubble size classes. The calculation of coalescence and fragmentation frequencies may therefore result in large errors, if the corresponding constitutive equations are based on bubble densities averaged over the cross section.

References

[1] A. Tomiyama, Struggle with computational bubble dynamics, in: Proceedings of Third International Conference on Multiphase Flow, ICMF 98, Lyon, France, June 8–12, 1998.

[2] H.-M. Prasser, A. Böttger, J. Zschau, A new electrode-mesh tomograph for gas-liquid flows, Flow Measurement and Instrumentation 9 (1998) 111–119.

[3] H.-M. Prasser, D. Scholz, C. Zippe, Bubble size measurement using wire-mesh sensors, Flow Measurement and Instrumentation 12 (4) (2001) 299–312.

[4] A.-K. Krüssenberg, H.-M. Prasser, A. Schaffrath, A new criterion for the identification of the bubble slug transition in vertical tubes, Kerntechnik 65 (1) (2000) 7–13.